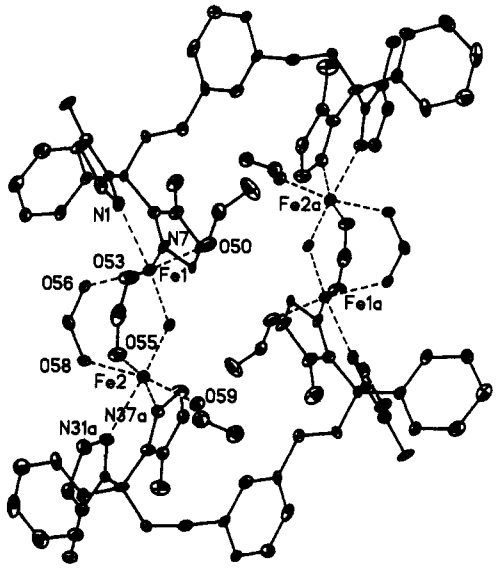

Figure 1. View of $[Fe_4O_2(C_{76}N_{16}O_4)(CHO_2)_8]$. H atoms are omitted for clarity. Ellipsoids scaled to the 20% probability level. The complex lies around an inversion center located between the Fe dimers. The coordination around each Fe is octahedral and is indicated by the dashed lines. The Fe atoms in the dimer are bridged by two formates and an oxide with an Fe-Fe separation of 3.221 (2) Å. Each Fe is also coordinated by two imidazole nitrogens and a monodentate formate. Relevant Fe bond lengths (Å) are as follows: Fe1-N1, 2.209 (12); Fe1-N7, 2.111 (11); Fe1-O49, 1.807 (8); Fe1-O50, 2.003 (12); Fe1-O53, 2.058 (11); Fe1-O56, 2.142 (9); Fe2-O49, 1.811 (8); Fe2-O55, 2.057 (11); Fe2-O58, 2.088 (9); Fe2-O59, 2.027 (11); Fe2-N31a, 2.206 (11); Fe2-N37a, 2.115 (11). The Fe-Fe distances between the diiron cores are 7.176 (6) (Fe1-Fe2a) and 7.790 (4) Å (Fe1-Fe1a). Relevant bond angles (deg) are as follows: Fe1-O49-Fe2, 125.9 (5); N1-Fe1-O49, 172.2 (4); O56-Fe1-O50, 170.1 (4); O53-Fe1-N7, 165.6 (4); N1-Fe1-O50, 89.9 (4); N1-Fe1-O53, 84.1 (4); N1-Fe1-O56, 80.7 (4); N1-Fe1-N7, 81.5 (4); O49-Fe1-O56, 92.2 (4); O49-Fe1-O53, 98.9 (4); O49-Fe1-O50, 97.3 (4); O49-Fe1-N7, 95.5 (4); N31a-Fe2-O49, 175.4 (4); N37a-Fe2-O55, 165.4 (4); O58-Fe2-O59, 169.7 (4); N31a-Fe2-O55, 84.0 (4); N31a-Fe2-O58, 82.2 (4); N31a-Fe2-O59, 87.6 (4); N31a-Fe2-N37a, 81.5 (4); O49-Fe2-O59, 96.7 (4); O49-Fe2-O58, 93.5 (4); O49-Fe2-O55, 97.2 (4); O49-Fe2-N37a, 97.2 (4). Atoms labeled with an a are related by $1-x, -y, -z$.

the iron complex formed using either of the above processes result in the formation of green crystals of **2**.

The single-crystal X-ray analysis of **2** revealed a tetrameric iron complex $[Fe_2O(O_2CH)_4L_2]_2 \cdot 4MeOH \cdot 2CHCl_3$, as shown in Figure 1. The complex contains the familiar (μ-oxo)bis(μ-carboxylato)diiron(III) core. Each iron is in an approximate octahedral coordination environment with the outer faces of the diiron core capped by the imidazoles and monodentate formates. Interestingly, the rigid xylylene bridge does not link the iron centers by bridging the (μ-oxo)bis(μ-formato)diiron(III) core, as one might expect for dimer formation. Instead the two dinuclear cores are linked via the bridge to form a tetranuclear complex with the distances between the cores found to be 7.176 (6) (Fe1-Fe2a) and 7.790 (4) (Fe1-Fe1a) Å.

The similarity between the monomeric and dimeric imidazole-containing ligands, L_1 and L_2, respectively, makes a comparison of the diiron cores of interest. With the obvious exception that L_2 stabilizes a tetrameric complex and L_1, a dimer, the key features of these two ligand-stabilized complexes are remarkably similar. Table III allows for a comparison between complexes **2**, formed from L_2, and **3** $[Fe_2(\mu\text{-}O)(\mu\text{-}O_2CH)_4(L_1)_2]$, the diferric complex of L_1.[9] The Fe-Fe distance within the core of **2** (3.221 (2) Å) is slightly longer than that of **3** (3.201 (3) Å) and nearly the same as that of azidomethemerythrin (3.23 Å). A similar result is also seen for the Fe-N bond trans to the μ-oxo bridge. The bond is lengthened slightly in **2** (2.209 (12) Å versus 2.16 (1) Å for **3**) but is still shorter than that of the protein (2.24 Å). An interesting difference between **2** and **3**, however, is seen in the positioning of the monodentate formates. The end-on formates in complex

Table III. Structural and Spectroscopic Data for **2**, **3**, and Azidomethemerythrin

	2	**3**	azidomethemerythrin
Fe-O (μ-oxo) (avg), Å	1.809 (8)	1.79 (1)	1.79
cis-Fe-N (avg), Å	2.113 (11)	2.12 (2)	2.13
Fe-O (μ-formate) (avg), Å	2.058 (11),[b] 2.115 (9)[c]	2.06 (1),[b] 2.10 (1)[c]	
Fe-O (end-on formate) (avg), Å	2.015 (12)	2.02 (1)	
trans-Fe-N (avg), Å	2.209 (12)	2.16 (1)	2.24
Fe-Fe within core, Å	3.221 (2)	3.201 (3)	3.23
Fe-O-Fe, deg	125.9 (5)	127.0 (6)	130
λ_{max}, nm (ϵ_M/Fe, cm^{-1} mol^{-1})[a]	662 (8)	662 (70)	680 (95)
	518 (sh)	520 (sh)	
	482 (sh, 350)	478 (sh)	
	448 (sh, 370)	448 (370)	446 (1850)
	356 (sh, 3100)	354 (sh, 2900)	380 (sh)
	332 (3350)	329 (3400)	326 (3375)
refs	this work	9	2, 3

[a] Solvent for **2** and **3**, chloroform. [b] Cis to end-on formate. [c] Trans to end-on formate.

3 are found to lie on opposite sides of a plane drawn through the Fe-O-Fe center, whereas, in **2**, the formates are constrained by the ligand to sit in a cis disposition.

In conclusion, we have synthesized a new ligand capable of binding two metals in a biomimetic environment. The formation of a tetrameric iron(III) complex suggests that dimeric metal complexes are not ensured by the use of rigid linkers. In the present case, it is possible that the 2 H of the xylene bridge is sufficient to inhibit dimer formation and that a directing influence, such as a phenoxide bridge, may be necessary to coerce the irons into forming a dimer.[16] We are presently synthesizing ligands that may allow us to explore such a possibility.

Acknowledgment. We are grateful to the National Institutes of Health (Grant No. GM 36348) for financial support of this research.

Supplementary Material Available: View of the asymmetric unit, showing the atom labeling scheme, and the unit cell packing diagram (Figures S1 and S2), listings of positional and isotropic thermal parameters for the H atoms (Table S1), anisotropic thermal parameters for the non-hydrogen atoms (Table S2), bond lengths and angles for the non-hydrogen atoms (Tables S3 and S4), and bond lengths and angles for the H atoms (Tables S5 and S6), and an X-ray experimental summary (16 pages); a listing of observed and calculated structure factor amplitudes (Table S7) (24 pages). Ordering information is given on any current masthead page.

(16) Many cases of dimeric metal complexes with bridging phenoxides have been reported. See: Borovik, A. S.; Papaefthymiou, V.; Taylor, L. F.; Anderson, O. P.; Que, L., Jr. *J. Am. Chem. Soc.* **1989**, *111*, 6183-6195 and references cited therein.

Contribution from the Department of Chemistry, University of Houston, Houston, Texas 77204-5641

Electrochemical, Spectroscopic, and Structural Characterization of $Rh_2(dpf)_4$, $Rh_2(dpf)_4(CH_3CN)$, and $[Rh_2(dpf)_4(CH_3CN)]ClO_4$, Where dpf = *N*,*N*'-Diphenylformamidinate(1-)

J. L. Bear,* C.-L. Yao, R. S. Lifsey, J. D. Korp, and K. M. Kadish*

Received January 30, 1990

Virtually all electron-rich dirhodium(II) tetraamidate or tetraamidinate complexes undergo two metal-centered one-electron oxidations.[1-7] Electroreductions of these complexes are generally

not observed, but several exceptions have been noted in the literature. For example, tetrakis(μ-*N*,*N*'-diphenylbenzamidinato)dirhodium(II), $Rh_2(dpb)_4$,[6] and $Rh_2(form)_4$,[7] where form = *N*,*N*'-di-*p*-tolylformamidinate(1−), can both be reduced in a reversible one-electron-transfer step to generate a stable Rh^IRh^{II} species. The reduction of $[Rh_2(O_2CCH_3)_n(L)_{4-n}]^{(4-n)+}$, where L is a neutral multidentate ligand containing the 1,8-naphthyridine fragment, has also been reported, but this reaction occurs at the ligand, rather than at the metal center.[8-10]

N,*N*'-Diphenylamidinate bridging ions are known to stabilize higher oxidation states of the dirhodium unit, and the formation of a mixed-valent Rh^IRh^{II} complex upon reduction of the $Rh_2(L)_4$ complex was unexpected. Also, since these were the only examples for dirhodium complexes of Rh^IRh^{II}, it was not clear how the bridging ligands might contribute to a stabilization of this mixed-valent state species. The reduction of $Rh_2(dpb)_4$ is metal centered, and both the *g* values in the ESR spectrum[11,12] and theory[13,14] suggest that the LUMO is σ^*_{Rh-Rh}.

The energy of the σ^*_{Rh-Rh} orbital should be extremely sensitive to axial interactions, and the ability of the bridging ligands to restrict axial ligation might be a major factor influencing the formation and stability of a Rh^IRh^{II} complex. However, almost nothing was known about how axial ligation would affect the metal oxidation state or the molecular structures of dirhodium *N*,*N*'-diphenylamidinate complexes. It was also not known how steric factors might control the axial site reactivity. This is discussed in the present paper, which compares molecular structures, ligand binding properties, and electrochemistry of $Rh_2(dpf)_4$ (**1**), $Rh_2(dpf)_4(CH_3CN)$ (**1L**), and $[Rh_2(dpf)_4(CH_3CN)]^+$ (**1L**$^+$) (dpf = *N*,*N*'-diphenylformamidinate(1−)).

Experimental Section

Chemicals. Rhodium(II) acetate was synthesized from $RhCl_3 \cdot 3H_2O$ (Matthey Bishop) by a known procedure.[15] *N*,*N*'-Diphenylformamidine (98%, mp = 140 °C) was purchased from Aldrich Chemical Co. and recrystallized from CH_2Cl_2 prior to use. Spectroscopic grade CH_2Cl_2 and CH_3CN were dried by distillation over CaH_2. Tetra-*n*-butylammonium perchlorate (TBAP) was recrystallized from ethanol and vacuum-dried. Tetra-*n*-butylammonium chloride and cyanide, (TBA)Cl and (TBA)CN, were purchased from Fluka Chemical Co. and stored under nitrogen in a drybox.

Instrumentation. Electronic absorption spectra were obtained with a Perkin-Elmer 330 UV–visible spectrophotometer. ESR measurements were made with an IBM Model 100D ESR spectrometer. An IBM 225 voltammetric analyzer was used for electrochemical studies. The electrochemical cell consisted of a platinum-button working electrode, a platinum-wire auxiliary electrode, and a saturated calomel reference electrode (SCE).

$Rh_2(dpf)_4$ (1). A mixture of H(dpf) (17.8 g, 90.7 mmol) and $Rh_2(O_2CCH_3)_4$ (0.5 g, 1.13 mmol) was heated in an oil bath at 130 °C for 10 h under vacuum. After cooling, the excess ligand was removed by repeated washing with CH_3OH, leaving an insoluble green solid, which was purified by column chromatography (silica gel, CH_2Cl_2 eluent). The yield was 90%. Large greenish black crystals were deposited upon evaporation of a CH_2Cl_2 solution, and a square plate of dimensions 0.50 × 0.50 × 0.08 mm was used for X-ray analysis.

$Rh_2(dpf)_4(CH_3CN)$ (1L). Slow evaporation of a CH_3CN solution of **1** (10.0 mg/50 mL) over the course of 4–5 days gave large purple-black crystals. A fragment of dimensions 0.60 × 0.50 × 0.15 mm was cut from a large crystal and used for X-ray analysis.

$[Rh_2(dpf)_4(CH_3CN)]ClO_4$ ($1L^+ClO_4^-$). A solution of **1** (0.5 mM) in $C_2H_4Cl_2$ containing 0.1 M TBAP was bulk-electrolyzed at 0.65 V. The solvent was then removed with a rotary evaporator and TBAP separated on a silica gel column using CH_2Cl_2 as eluent. Slow evaporation of a CH_3CN solution produced small reddish black crystals. A crystal of dimensions 0.35 × 0.35 × 0.15 mm was chosen for X-ray analysis.

X-ray Data Collection. Crystals of each complex were mounted on a glass fiber in a random orientation on an Enraf-Nonius CAD-4 automatic diffractometer. The radiation used was Mo Kα monochromatized by a dense graphite crystal assumed for all purposes to be 50% imperfect. Intensities were measured using the θ–2θ scan technique, with the scan rate depending on the net count obtained in rapid prescans of each reflection. Two standard reflections were monitored periodically during the course of each data collection as a check of crystal stability and electronic reliability, and did not vary significantly. Lorentz and polarization corrections were applied; however, no corrections for absorption were made due to the small absorption coefficients (**1**, 7.84 cm^{-1}; **1L**, 7.36 cm^{-1}; **1L**$^+$, 7.6 cm^{-1}). Structures were solved by using either the Patterson method or MULTAN. After all shift/esd ratios were less than 0.1, convergence was reached with the following *R* values: **1** [$R(F_o)$ = 0.028, $R_w(F_o)$ = 0.028], **1L** [$R(F_o)$ = 0.039, $R_w(F_o)$ = 0.040], **1L**$^+$ [$R(F_o)$ = 0.042, $R_w(F_o)$ = 0.045]. All calculations were made by using the Molecular Structure Corp. TEXRAY 230 modifications of the SDP-PLUS series of programs. Compound **1** ($Rh_2N_8C_{52}H_{44}$) crystallizes in space group $P2/n$ with 4 formula weights in a unit cell of dimensions a = 17.881 (9) Å, b = 10.273 (2) Å, c = 24.419 (7) Å, and β = 101.793 (3)°. Both **1L** ($Rh_2N_9C_{54}H_{47}$) and **1L**$^+$ ($(Rh_2N_9C_{54}H_{47}^+)(ClO_4^-)$) crystallize in space group $P4/ncc$ with 4 formula weights in the unit cell. The lattice constants are a = 13.659 (6) Å and c = 25.199 (7) Å for the former complex and a = 14.308 (4) Å and c = 24.314 (6) Å for the latter.

The asymmetric unit of **1** consists of two half-molecules, both situated on a 2-fold axis that runs perpendicular to the metal–metal bond and passes obliquely between the attached ligands. Although crystallographically independent, both molecules possess essentially the same geometry. In both **1L** and **1L**$^+$, the dirhodium molecule is situated on a 4-fold axis. This necessarily implies complete disorder of the acetonitrile hydrogens, and no attempt was made to locate or refine them. In **1L**$^+$, the perchlorate anion was found to be situated on a 222 symmetry

Table I. Selected Bond Lengths (Å) and Angles (deg) for **1**, **1L**, and **1L**$^+$ [a]

	1	1L	1L$^+$
	Lengths		
Rh–Rh	2.457 (1)	2.459 (1)	2.466 (1)
Rh–N(1)	2.057/2.038 (4)	2.062 (2)	2.035 (4)
Rh–N(2)		2.066 (2)	2.025 (4)
Rh–N(3)[b]		2.106 (4)	2.074 (6)
N(1)–C(1)	1.314 (6)	1.307 (2)	1.303 (5)
N(2)–C(1)		1.324 (3)	1.338 (5)
N(1)–C(2)	1.419 (6)	1.420 (3)	1.456 (5)
N(2)–C(8)		1.418 (3)	1.420 (5)
N(3)–C(14)		1.113 (5)	1.127 (9)
C(14)–C(15)		1.523 (7)	1.461 (12)
	Angles		
Rh–Rh–N(1)	88.0 (1)	86.4 (5)	86.9 (1)
Rh–Rh–N(2)		87.3 (5)	87.8 (1)
Rh–Rh–N(3)[b]		180	180
Rh–N(1)–C(1)	119.9 (4)	120.0 (2)	120.4 (3)
Rh–N(1)–C(2)	121.8 (4)	122.2 (1)	123.0 (3)
C(1)–N(1)–C(2)	117.9 (5)	117.6 (2)	116.0 (4)
Rh–N(2)–C(1)		118.2 (2)	118.9 (3)
Rh–N(2)–C(8)		122.9 (2)	123.8 (3)
C(1)–N(2)–C(8)		118.9 (2)	117.2 (4)
N(1)–C(1)–N(2)	123.7 (5)	122.9 (2)	123.0 (4)
N–Rh–Rh–N	3.5	16.8	12.5
C(3)–C(2)–N(1)–C(1)	60.5/27.9	70.7	70.3
C(9)–C(8)–N(2)–C(1)	27.9/60.5	43.0	42.8

[a] For **1**, the average of chemically equivalent values is given. [b] The side where CH_3CN is bound to **1L** and **1L**$^+$.

(1) Duncan, J.; Malinski, T.; Zhu, T. P.; Hu, Z. S.; Kadish, K. M.; Bear, J. L. *J. Am. Chem. Soc.* **1982**, *104*, 5507.
(2) Bear, J. L.; Zhu, T. P.; Malinski, T.; Dennis, A. M.; Kadish, K. M. *Inorg. Chem.* **1984**, *23*, 674.
(3) Zhu, T. P.; Ahsan, M. Q.; Malinski, T.; Kadish, K. M.; Bear, J. L. *Inorg. Chem.* **1984**, *23*, 2.
(4) Chavan, M. Y.; Zhu, T. P.; Lin, X. Q.; Ahsan, M. Q.; Bear, J. L.; Kadish, K. M. *Inorg. Chem.* **1984**, *23*, 4538.
(5) Bear, J. L.; Liu, L.-M.; Kadish, K. M. *Inorg. Chem.* **1987**, *26*, 2927.
(6) Le, J. C.; Chavan, M. Y.; Chau, L. K.; Bear, J. L.; Kadish, K. M. *J. Am. Chem. Soc.* **1985**, *107*, 7195.
(7) Piraino, P.; Bruno, G.; Schiavo, S. L.; Laschi, F.; Zanello, P. *Inorg. Chem.* **1987**, *26*, 2205.
(8) Tikkanen, W. R.; Binamira-Soriaga, E.; Kaska, W. C.; Ford, P. C. *Inorg. Chem.* **1983**, *22*, 1147.
(9) Tikkanen, W. R.; Binamira-Soriaga, E.; Kaska, W. C.; Ford, P. C. *Inorg. Chem.* **1984**, *23*, 141.
(10) Bear, J. L.; Chau, L. K.; Chavan, M. Y.; Lefoulon, F.; Thummel, R. P.; Kadish, K. M. *Inorg. Chem.* **1986**, *25*, 1514.
(11) Kawamura, T.; Fukamachi, K.; Sowa, T.; Hayashida, S.; Yonezawa, T. *J. Am. Chem. Soc.* **1981**, *103*, 364.
(12) Kawamura, T.; Katayama, H.; Yamabe, T. *J. Am. Chem. Soc.* **1989**, *111*, 8156.
(13) Rizzi, G. A.; Casarin, M.; Tondello, E.; Piraino, P.; Granozzi, G. *Inorg. Chem.* **1987**, *26*, 3406.
(14) Cotton, F. A.; Feng, X. *Inorg. Chem.* **1989**, *28*, 1180.
(15) Rampel, G. A.; Legzdens, P.; Smith, H.; Wilkinson, G. *Inorg. Synth.* **1972**, *13*, 90.

Table II. Atomic Coordinates (×10⁴) of Core Atoms

atom	x	y	z
	$Rh_2(dpf)_4$ (**1**)		
Rh(1)	7673 (1)	2274 (1)	7038 (1)
Rh(2)	7364 (1)	−111 (1)	2973 (1)
N(1)	6855 (3)	899 (5)	6775 (2)
N(2)	6576 (3)	805 (4)	7655 (2)
N(3)	6881 (3)	3736 (5)	6812 (2)
N(4)	6516 (3)	3639 (5)	7673 (2)
N(5)	8162 (3)	1355 (5)	3156 (2)
N(6)	8462 (3)	1256 (5)	2281 (2)
N(7)	8192 (3)	−1477 (5)	3199 (2)
N(8)	8407 (3)	−1571 (5)	2293 (2)
C(1)	6492 (4)	373 (6)	7143 (3)
C(14)	6474 (4)	4140 (6)	7168 (3)
C(27)	8530 (4)	1764 (6)	2775 (3)
C(40)	8529 (4)	−1976 (6)	2809 (3)
	$Rh_2(dpf)_4(CH_3CN)$ (**1L**)		
Rh(1)	2500	2500	2482 (1)
Rh(2)	2500	2500	3458 (1)
N(1)	1336 (3)	1543 (3)	2534 (1)
N(2)	1660 (3)	1244 (3)	3419 (1)
N(3)	2500	2500	1646 (3)
C(1)	1178 (4)	1063 (4)	2974 (1)
C(14)	2500	2500	1204 (3)
C(15)	2500	2500	600 (4)
	$[Rh_2(dpf)_4(CH_3CN)]ClO_4$ (**1L**$^+ClO_4^-$)		
Rh(1)	7500	7500	2432 (1)
Rh(2)	7500	7500	3446 (1)
N(1)	8348 (5)	8639 (4)	2476 (2)
N(2)	8078 (5)	8790 (5)	3413 (3)
N(3)	7500	7500	1579 (5)
C(1)	8453 (6)	9084 (6)	2940 (3)
C(14)	7500	7500	1115 (7)
C(15)	7500	7500	514 (7)

site, with massively disordered oxygens. Only the four positions having the highest amount of electron density were refined as oxygens, each with a population factor of 25%.

Determination of Binding Constants for Axial Ligation. Formation constants for the binding of Cl^-, CN^-, and CH_3CN by $[Rh_2(dpf)_4]^n$ (n = 0, +, and 2+) were determined as previously described[16] by using standard spectrophotometric and electrochemical methodologies.

Results and Discussion

Structures of 1, 1L, and 1L$^+$. The structures of **1** and **1L** are shown in Figure 1. The general structure features of **1L**$^+$ are essentially the same as those of **1L**. Selected bond lengths and angles of all three complexes are given in Table I, and the atomic coordinates of the significant atoms are listed in Table II. The Rh–Rh bond distance of 2.457 (1) Å for **1** is longer than that of $Rh_2(dpb)_4$ (2.389 (1) Å) or $Rh_2(form)_4$ (2.4336 (4) Å) but falls midway in the range of other dirhodium(II) complexes.[5-9,17-20] There are two different bonding arrangements on each Rh atom. One of the Rh–N average bond lengths is 2.037 Å, while the other is 2.057 Å. The phenyl group on the nitrogen atom that has the shorter Rh–N bond is ~28° out of the plane of the bridging ligand, whereas the other phenyl group is twisted ~60° out of the plane. The N–Rh–Rh–N torsion angle is 3.5°, much smaller than the ~17° angle observed for $Rh_2(dpb)_4$ and $Rh_2(form)_4$. Therefore, the difference in the N–Rh–Rh–N torsion angles for these complexes is not explained by steric factors.

The Rh–Rh bond length in **1L** is 2.459 (1) Å, essentially the same as in **1**. However, there are significant changes in the other bond lengths and angles. All of the Rh–N(eq) bond lengths for **1L** are approximately equal and quite long, averaging 2.064 Å. The Rh–N(ax) distance is 2.106 (4) Å and is short compared to the 2.254 (7) Å found for the bis(acetonitrile) adduct $Rh_2(O_2CCH_3)_4(CH_3CN)_2$.[17] In **1L** the four phenyls that surround the axial CH_3CN are 70° out-of-plane, while on the other side of the molecule they are twisted by 43°. Axial ligation results in a 16.8° torsional twist of the Rh equatorial planes.

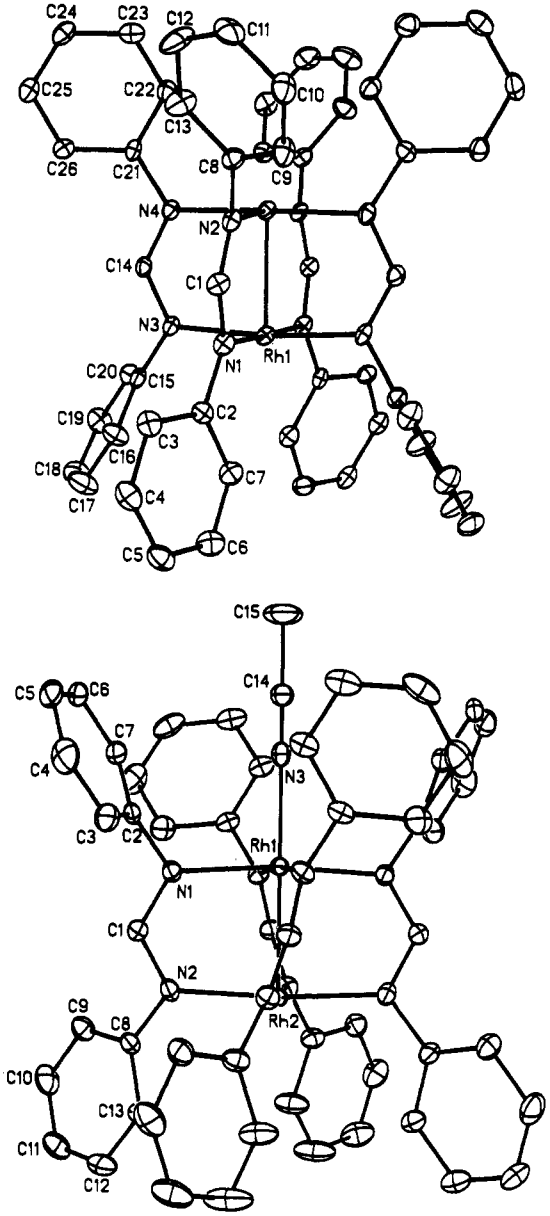

Figure 1. Labeled diagrams of (top) $Rh_2(dpf)_4$ (**1**) and (bottom) $Rh_2(dpf)_4(CH_3CN)$ (**1L**).

The structure of **1L**$^+$ is similar to that of **1L**. The Rh–Rh bond length of 2.466 (1) Å is slightly longer, while the Rh–N(ax) and average Rh–N(eq) bond distances decrease by 0.032 and 0.034 Å, respectively, compared to those of **1L**. The average N–C(Ph) distance in both **1** and **1L** is 1.419 Å. However, in **1L**$^+$, this distance increases to 1.456 (5) Å for the *N*-phenyl groups bound to the rhodium atom with the axial ligand. Such an increase is probably related to the loss of an electron from the $\delta^*_{Rh-Rh}\pi^*_{Rh-N}$ orbital (HOMO). It is not clear why there is a decrease in the torsion angle from 16.8 to 12.5° upon oxidation of **1L**.

Electrochemistry of $Rh_2(dpf)_4$. $Rh_2(dpf)_4$ in CH_2Cl_2, 0.1 M TBAP under Ar undergoes two reversible one-electron oxidations ($E_{1/2}$ = 0.34 and 1.15 V) and a reversible one-electron reduction ($E_{1/2}$ = −1.21 V). Reversible oxidations are also observed in CH_3CN, and these occur at $E_{1/2}$ = 0.12 and 0.95 V (see Figure 2a). The cathodic shift of $E_{1/2}$ from values in CH_2Cl_2 is consistent with an increase in electron density on the dirhodium unit and results from axial coordination by CH_3CN. The single reduction

(16) Chavan, M. Y.; Lin, X. Q.; Ahsan, M. Q.; Bear, J. L.; Kadish, K. M. *Inorg. Chem.* **1986**, *25*, 1281.
(17) Felthouse, T. R. *Prog. Inorg. Chem.* **1982**, *29*, 73.
(18) Piraino, P.; Bruno, G.; Tresoldi, G.; Schiavo, S. L.; Nicolo, F. *Inorg. Chem.* **1989**, *28*, 139.
(19) Boyar, E. B.; Robinson, S. D.; *Coord. Chem. Rev.* **1983**, *50*, 109.
(20) Cotton, F. A.; Walton, R. A. *Multiple Bonds Between Metal Atoms*; John Wiley and Sons: New York, 1982.

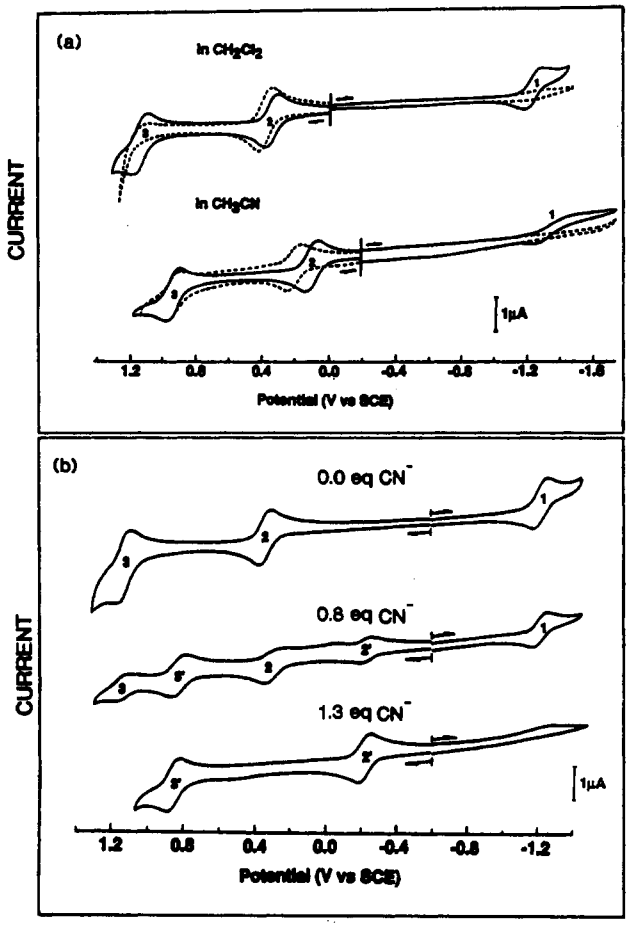

Figure 2. Cyclic voltammograms of (a) $Rh_2(dpf)_4$ in CH_2Cl_2 and CH_3CN, 0.1 M TBAP under Ar (solid line) and under CO (dashed line) and (b) 3.0×10^{-4} M $Rh_2(dpf)_4$ in CH_2Cl_2, containing 0.1 M TBAP and 0.0–1.3 equiv of (TBA)CN. Scan rate = 0.1 V/s.

of $Rh_2(dpf)_4$ in CH_3CN becomes quasireversible and occurs at $E_{pc} = -1.40$ V for a scan rate of 0.1 V/s.

Bulk controlled-potential oxidation and rereduction of $Rh_2(dpf)_4$ at 0.65 and 0.00 V in CH_2Cl_2 or CH_3CN under Ar reversibly gives 1.0 ± 0.1 electrons transferred. The electroreduction of $Rh_2(dpf)_4$ at −1.50 V in CH_3CN involves the addition of 1.0 ± 0.2 electrons and gives a stable radical anion. However, a similar electroreduction carried out in CH_2Cl_2 involves a multielectron transfer and the residual current remains high even after 30 min of electrolysis. This suggests that $[Rh_2(dpf)_4]^-$ reacts rapidly with the chlorinated hydrocarbon solvent.

A green to pink color change occurs when CO is bubbled through CH_2Cl_2 or CH_3CN solutions containing **1**. The first oxidation in CH_3CN shifts from $E_{1/2} = 0.12$ V under Ar (solid line, Figure 2a) to 0.20 V under CO (dashed line, Figure 2a). The second oxidation of **1** remains unchanged, but the reduction process that is assigned as the formation of $Rh^{II}Rh^{I}$ under Ar disappears under a CO atmosphere. The first oxidation of $Rh_2(dpf)_4$ shifts by 30 mV (from 0.34 to 0.37 V) in CH_2Cl_2 when Ar is replaced by CO (see Figure 2a). The potentials for both the first reduction and the second oxidation of **1** both shift completely out of the potential window in CH_2Cl_2 saturated with CO. The decreased anodic potential limit of CH_2Cl_2 is due to the oxidation of free CO, which occurs at ~1.3 V. The data for $Rh_2(dpf)_4$ can be compared with data for $Rh_2(form)_4$, which, upon CO binding, undergoes a 0.04-V anodic potential shift in the first oxidation, a 0.17-V anodic potential shift in the second oxidation, and a 0.47-V cathodic potential shift in the first reduction.[7]

The binding of CO to dirhodium(II) complexes generally lowers the energy of the HOMO due to π back-bonding from the filled π^*_{Rh-Rh} MO to the empty π^*_{CO} MO. However the disappearance of the reduction wave upon CO binding to **1** shows that the LUMO of the monoadduct is considerably higher in energy than that of the unligated complex. This suggests that the energy of the LUMO is determined by the Rh–CO σ interaction, while that of the HOMO is determined by the Rh–CO π component.

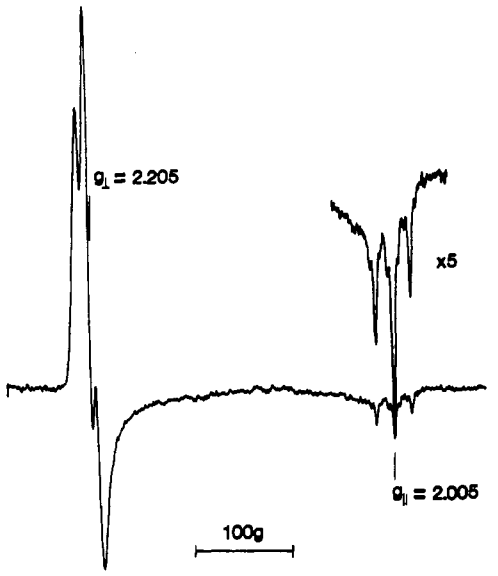

Figure 3. ESR spectrum of $[Rh_2(dpf)_4]^-$ (1^-) at 123 K in CH_2Cl_2, 0.1 M TBAP containing 1 M CH_3CN.

ESR Spectra. The ESR spectrum of $[Rh_2(dpf)_4]^+$ in CH_2Cl_2 under Ar shows an axial signal with $g_\perp = 2.071$ and $g_\parallel = 1.958$ at 123 K, the latter of which is split into a 1:2:1 triplet ($A_\parallel = 19.3 \times 10^{-4}$ cm^{-1}) by the two equivalent rhodium nuclei. The ESR spectrum of $[Rh_2(dpf)_4]^+$ in CH_3CN has a signal with $g_\perp = 2.077$ and $g_\parallel = 1.962$, which is split into a doublet of doublets ($A_\parallel = 22.4 \times 10^{-4}$ and 14.6×10^{-4} cm^{-1}). This indicates an unequal distribution of spin density on the two rhodium ions, which results from the axial binding of one CH_3CN molecule to $[Rh_2(dpf)_4]^+$ (see structural data).

The ESR spectrum of $[Rh_2(dpf)_4]^+$ in CH_2Cl_2 containing 1 equiv of CN^- or Cl^- has a $g_\parallel$ signal that is also split into a doublet of doublets, but in the presence of excess Cl^-, the ESR spectrum ($g_\perp = 2.085$ and $g_\parallel = 1.949$) shows a 1:2:1 triplet for $g_\parallel$, thus suggesting the formation of the bis adduct, $[Rh_2(dpf)_4Cl_2]^-$.

The ESR spectrum of $[Rh_2(dpf)_4]^-$ in CH_2Cl_2 containing ~0.01 M CH_3CN is shown in Figure 3. There is a signal at $g_\perp = 2.205$ ($A_\perp = 11.1 \times 10^{-4}$ cm^{-1}) and $g_\parallel = 2.005$ ($A_\parallel = 16.8 \times 10^{-4}$ cm^{-1}, $A_N = 4.7 \times 10^{-1}$ cm^{-1}). The spectrum (Figure 3) is similar to one reported for $[Rh_2(dpb)_4(CH_3CN)]^-$ ($g_\perp = 2.181$, $A_\perp = 9 \times 10^{-4}$ cm^{-1}, $g_\parallel = 2.003$, $A_\parallel = 16 \times 10^{-4}$ cm^{-1}) and is assigned to $[Rh_2(dpf)_4(CH_3CN)]^-$. The values of $g_\perp$ and $g_\parallel$ are split into 1:2:1 triplets for both dirhodium complexes, and $g_\parallel$ displays hyperfine coupling. The observed hyperfine coupling of nitrogen and the fact that $g_\parallel < g_e$[11,12] show that CH_3CN is axially bound to the $Rh^{I}Rh^{II}$ unit and indicate that the SOMO of $[Rh_2(dpf)_4(CH_3CN)]^-$ is the $\sigma^*_{Rh-Rh}\sigma^*_{Rh-L}$ molecular orbital.

Complexation of $Rh_2(dpf)_4$ and $[Rh(dpf)_4]^+$ with Cl^-, CN^-, or CH_3CN. Figure 4a shows the UV–visible spectral changes that occur upon addition of CH_3CN to $Rh_2(dpf)_4$ in CH_2Cl_2. The spectral data were analyzed at 470 and 880 nm and gave plots of the type shown in the insert of Figure 4a. The experimental slope of 0.9 ± 0.1 is consistent with complexation of one CH_3CN ligand by $Rh_2(dpf)_4$ and gives a binding constant of 58.

A titration of $Rh_2(dpf)_4$ with (TBA)CN in CH_2Cl_2 indicates monoligation of CN^- ($n = 1.0 \pm 0.1$) and gives a calculated formation constant of 7.0×10^4. Chloride ions do not bind to neutral $Rh_2(dpf)_4$ in CH_2Cl_2, but $Rh_2(dpf)_4Cl$ is readily formed during titrations of the oxidized species with (TBA)Cl (see Figure 4b). A plot of the maximum absorption at 890 nm vs log $[Cl^-]$ clearly shows a two-step ligation of Cl^- to 1^+. A formation constant of 8.2×10^3 was calculated for the first ligand addition by using data of the type shown in the insert of Figure 4b. The formation constant for binding of a second Cl^- ion to 1^+ was not calculated, since an A_∞ value for $[Rh_2(dpf)_4Cl_2]^-$ could not be

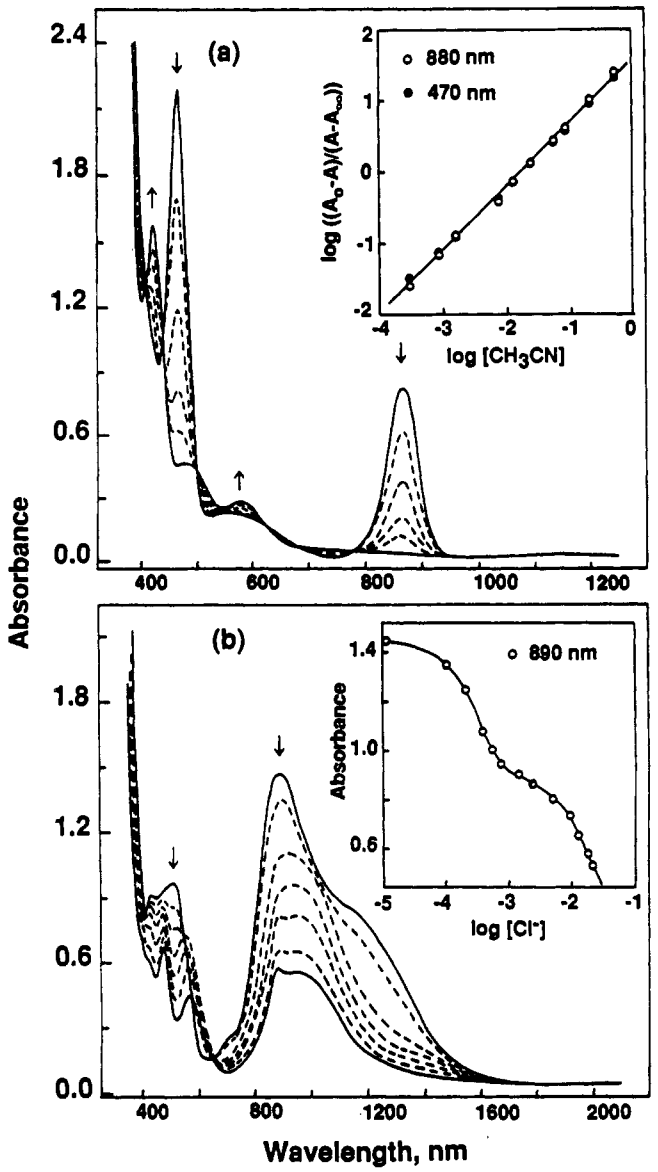

Figure 4. (a) Changes in the electronic absorption spectra of $Rh_2(dpf)_4$ in CH_2Cl_2 during titration with CH_3CN. The insert shows analysis of spectral data at 470 (•) and 880 (o) nm. (b) Changes in the electronic absorption spectra of $[Rh_2(dpf)_4]^+$ during titration with (TBA)Cl. The insert is a plot of absorption at 890 nm vs log $[Cl^-]$.

obtained, even up to the addition of 100 equiv of Cl^-.

Figure 2b shows cyclic voltammograms of **1** in CH_2Cl_2 containing different concentrations of (TBA)CN. The binding of CN^- to $Rh_2(dpf)_4$ and $[Rh_2(dpf)_4]^+$ is accompanied by a decrease in currents for the processes at 0.34, 1.15, and −1.21 V, as two new waves appear at $E_{1/2}$ = −0.20 and 0.86 V. The second oxidation (process 3) completely disappears when 1 equiv of CN^- is added to solution, but an irreversible wave at 0.34 V (process 2) still exists under these conditions. This suggests an incomplete formation of $[Rh_2(dpf)_4(CN)]^-$, but there is a quantitative conversion to $Rh_2(dpf)_4(CN)$ after the first oxidation. The first oxidation and the first reduction of **1** both completely disappear upon addition of about 1.3 equiv of CN^- to solution.

The binding of CN^- to $Rh_2(dpf)_4$ strongly destabilizes both the LUMO and the HOMO of the complex. The relative magnitude of K_1 vs K_1' (K and K' are the formation constants for $[Rh^{II}_2(dpf)_4(CN)]^-$ and $[Rh^{II}Rh^{III}(dpf)_4(CN)]$) is given by $E_{1/2}' = E_{1/2} + (RT/nF)\log(K_1/K_1')$ where $E_{1/2}$ and $E_{1/2}'$ are half-wave potentials for the $[Rh^{II}_2(dpf)_4]/[Rh^{II}Rh^{III}(dpf)_4]^+$ and $[Rh^{II}_2(dpf)_4(CN)]^-/[Rh^{II}Rh^{III}(dpf)_4(CN)]$ couples, respectively. The cathodic potential shift of 0.54 V for the first oxidation is associated with a K_1/K_1' ratio of 7.0×10^{-10}, and the cathodic shift of 0.29 V for the second oxidation is related to a K_1'/K_1'' ratio of 1.2×10^{-5} (K'' is the formation constant for $[Rh_2(dpf)_4(CN)]^+$). The value of K_1 for the conversion of $Rh_2(dpf)_4$ to $[Rh_2(dpf)_4(CN)]^-$ was calculated as 7.0×10^4 from the UV-vis data, and this value was then used to obtain K_1' and K_1'', which were calculated as 1.0×10^{14} and 8.3×10^{18}, respectively.

A titration of **1** with (TBA)Cl was also carried out in CH_2Cl_2, 0.1 M TBAP. A cathodic shift of the second oxidation occurs as Cl^- is added to solution and is due to the formation of $Rh_2(dpf)_4Cl$. However, the first oxidation was always irreversible in the presence of Cl^-. The resulting voltammogram has an anodic peak at 0.31 V and a cathodic peak at −0.09 V, thus suggesting coordination of Cl^- by $\mathbf{1}^+$ but not by **1**. Binding constants for $Rh_2(dpf)_4(Cl)$ and $[Rh_2(dpf)_4(Cl)]^+$ were calculated as 8.2×10^3 and 3.2×10^8, while constants of 1.4×10^4 and 1.4×10^4 were calculated for the formation of $[Rh_2(dpf)_4(CH_3CN)]^+$ and $[Rh_2(dpf)_4(CH_3CN)]^{2+}$ from $[Rh_2(dpf)_4]^+$.

Summary. The structures of **1**, **1L**, and $\mathbf{1L}^+$ show that the Rh–Rh bond length is relatively insensitive to either axial ligation or change in formal oxidation state of the complex but that the Rh–N bond lengths and the N–Rh–Rh–N torsion angle are both sensitive to these perturbations. Complexation with CN^-, Cl^-, or CH_3CN stabilizes the higher oxidation states of the dirhodium species according to the order $CN^- > Cl^- > CH_3CN$. In contrast, a complexation with CO stabilizes Rh^{II}_2 but strongly destabilizes Rh^IRh^{II}. An axial polarization of the SOMO is reflected in the ESR spectra of $Rh^{II}Rh^{III}(dpf)_4(L)$ and the strong tendency for **1** to form only monoadducts. The reduction of $Rh_2(dpf)_4$ to $[Rh_2(dpf)_4]^-$ is metal centered, and the resulting product is structurally stable. $[Rh_2(dpf)_4]^-$ axially binds to CH_3CN, and the ESR spectrum of $[Rh_2(dpf)_4(CH_3CN)]^-$ is consistent with a $\sigma^*_{Rh-Rh}\sigma^*_{Rh-L}$ SOMO assignment where the odd electron is delocalized over the two rhodium centers and the nitrogen of the axially bound CH_3CN ligand.

Acknowledgment. This work was supported by the Robert A. Welch Foundation (J.L.B., Grant No. E-918; K.M.K., Grant No. E-680).

Supplementary Material Available: Tables SI–SIII, listing the UV–visible data, half-wave potentials, and ESR data for the various $Rh_2(dpf)_4$ adducts, and Tables SIV–SVII, listing data collection and processing parameters, atomic coordinates, hydrogen atomic coordinates, and anisotropic thermal parameters for **1**, **1L**, and $\mathbf{1L}^+$ (13 pages); Tables SVIII–SX, listing observed and calculated structure factors (57 pages). Ordering information is given on any current masthead page.

Contribution from the Departments of Inorganic Chemistry and Physical Chemistry, University of Melbourne, Parkville, Victoria 3052, Australia

Electronic Spectra of the Cations of Europium(II), Samarium(II), and Ytterbium(II) in Anhydrous Hydrogen Fluoride

Colin G. Barraclough, Russell W. Cockman, and Thomas A. O'Donnell*

Received May 1, 1990

Anhydrous hydrogen fluoride (AHF), the acidity of which has been deliberately enhanced by the addition of Lewis acids, has been shown to be an excellent solvent for solvated transition-metal cations in both "normal", e.g. Co^{2+} and Pr^{3+},[1] and unusually high oxidation states, e.g. Ag^{2+}.[2] Much of our work has further extended the known and expected resistance of AHF toward powerful oxidants such as Ag^{2+}. It would require a very powerful oxidant to produce F_2 from HF. However, we have also dem-

* To whom correspondence should be addressed at the Department of Inorganic Chemistry.

0020-1669/91/1330-0340$02.50/0